PHYSICAL REVIEW MATERIALS **3**, 026003 (2019)

Anomalous variations of spectral linewidth in internal excitonic quantum transitions of ultrafast resonantly excited single-walled carbon nanotubes

Liang Luo, Zhaoyu Liu, Xu Yang, Chirag Vaswani, Di Cheng, Joong-Mok Park, and Jigang Wang[*]
Department of Physics and Astronomy and Ames Laboratory, U.S. DOE, Iowa State University, Ames, Iowa 50011, USA

(Received 29 July 2018; published 28 February 2019)

How the exciton fine structure and spectral linewidth in single-walled carbon nanotubes (SWNTs) evolve after ultrafast photoexcitation is critical for both understanding the fundamental optoelectronic properties and the development of nanophotonic functional devices. Yet, studies so far have mostly detected a subset of excitons near the Brillouin-zone center due to symmetry and momentum restrictions of the interband optical probes used, such as photoluminescence and absorption. Here we use ultrafast terahertz spectroscopy to probe the excitonic spectral linewidth associated with internal quantum transition across the entire momentum K space in resonantly excited semiconducting SWNTs. The lowest-lying intraexcitonic transition surprisingly sharpens at both high pump fluence and initial times immediately following the photoexcitation. We attribute these anomalous variations in the spectral linewidth to the role of the dark state $1s(g)$ that influences the lifetime broadening of the bright state $1s(u)$, consistent with the temperature-dependent dephasing time with a crossover temperature set by the internal quantum level spacing of excitons.

DOI: 10.1103/PhysRevMaterials.3.026003

I. INTRODUCTION

Single-walled carbon nanotubes (SWNTs), with appealing optical and electronic properties [1,2], are not only ideal model one-dimensional (1D) systems for fundamental scientific studies [3,4], but have a great potential for novel applications, such as nanometer-scaled photodetectors, light emitters, and other optoelectronic devices [5–7]. It is well recognized that the optical and electronic properties of SWNTs are primarily dominated by Coulomb-bound electron-hole pairs, called excitons [8,9], which, due to strong 1D Coulomb interaction and reduced screening, have a large binding energy of hundreds of meV [10,11], as illustrated in Fig. 1, distinct from two-dimensional (2D) and three-dimensional systems with a binding energy of several meV [12–14]. The band structure of excitons, as described in a 1D hydrogen-atom-like model, is characterized by the center-of-mass momentum K and internal quantum numbers, such as $1s$, $2s$, $2p$, etc. The presence of two equivalent valleys K and K' arising from graphene lattice and Coulomb interaction split each state into even (g) and odd (u) symmetries [15,16]. They have slightly different energy on the order of several meV and correspond to optically dark and bright states, e.g., the lowest-lying states $1s(g)$ and $1s(u)$ shown in Fig. 1(b). Prior studies on excitons in carbon nanotubes focus primarily on the photoluminescence (PL) [17,18], absorption [19], energy levels [20,21], ultrafast formation and dynamics [22,23], improvement of low quantum yield [24], and lifetimes [16,25]. However, to the best of our knowledge, the ultrafast evolution of the exciton spectral linewidth of SWNTs is only studied near $K \approx 0$ by a limited number of techniques, e.g., utilizing near-infrared interband probe [26] or interband PL [27]. Particularly, there has been no report studying exciton spectral linewidth across the entire K space using the direct terahertz (THz) internal excitonic transition free from the symmetry and momentum restrictions of interband optical probes [22,23]. The ultrafast evolution of exciton spectral linewidth after photoexcitation is very crucial for deeper understanding of the photophysics of carbon nanotubes and the development of carbon-nanotube-based optoelectronic devices.

Optical pump and THz probe spectroscopy, illustrated in Fig. 1(a), represents one of the most versatile techniques, which is very sensitive to many quasiparticles, such as electrons, phonons, and excitons, and suitable to measure their ultrafast dynamics quantitatively [28,29]. The meV energy of THz photons (1 THz = 4.1 meV) is especially suitable to probe the SWNTs intraexcitonic transitions with a similar energy gap. Specifically, THz photons can couple directly to the $1s(g) \rightarrow 1s(u)$ intraexcitonic transition, i.e., between optically dark and bright ground states, across the entire center-of-mass momentum K space, as indicated by red arrows in Fig. 1(b). This is unlike conventional interband PL and absorption measurements, in which only a small portion of excitons near $K \approx 0$ is measured because of the symmetry restriction and small momentum of photons [25]. Therefore, THz pulses can measure ultrafast time-resolved exciton density and spectral linewidth involved in transition across the entire K space. These important aspects about excitons are absent from prior SWNT studies, especially under strong and resonant pumping regimes that generate a large density of excitons, although the internal excitonic transitions are well established [20,22,23].

In this paper, we use the unique quantitative intraexcitonic probe of nonequilibrium state to reveal anomalous variations in the spectral linewidth of the $1s(g) \rightarrow 1s(u)$ transition around 1.5 THz in individualized (6,5) SWNTs at low temperature $T = 5$ K. The absorption spectrum of the SWNTs film at room temperature displays both E_{11} and E_{22} excitonic absorption

---

[*] jgwang@iastate.edu

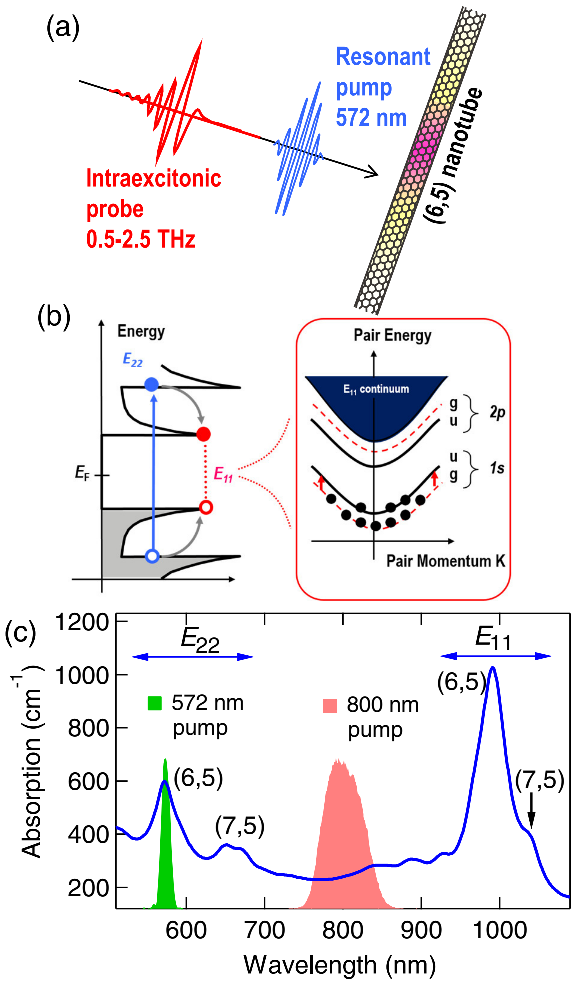

FIG. 1. THz measurement and sample characterization. (a) Schematic of the experiment and (b) the electronic energy dispersion of semiconducting SWNTs showing that 572-nm pump beam resonantly excites E_{22} excitons in (6,5) SWNTs (blue arrow) which is probed by subsequent THz beam via $1s(g) \rightarrow 1s(u)$ intraexcitonic transition (red arrows), from which exciton density and spectral linewidth are calculated. (c) Absorption spectrum (blue curve) of the SWNT film measured at room temperature showing both E_{11} and E_{22} excitonic absorption peaks of dominant (6,5) and (7,5) chiralities, e.g., E_{11} at 991 nm for (6,5) and at 1050 nm for (7,5), and E_{22} at 572 nm for (6,5) and at 652 nm for (7,5), respectively. Two pump spectra, 572 nm (green shade) and 800 nm (red shade), are also plotted.

peaks of dominant (6,5) and (7,5) chiralities, as shown in Fig. 1(c). The 572-nm pump spectrum (green shade) used for resonant excitation matches very well with the E_{22} band of (6,5) SWNTs, and the subsequent THz pulses probe the $1s(g) \rightarrow 1s(u)$ transition, whose spectral line shapes and amplitudes yield quantitatively the spectral linewidths and densities of photogenerated free charge carriers and lowest-lying excitons. We observe that the spectral linewidth of *free carriers* increases both with increasing pump fluence and at the initial delay time after photoexcitation, which is consistent with prior studies of normal semiconductor materials [12,30]. However, in strong contrast, the spectral linewidth of the $1s(g) \rightarrow 1s(u)$ internal *excitonic* transition surprisingly exhibits completely opposite behavior. We attribute this to excitation-induced competing channels in the $1s(g)/1s(u)$ exciton pair transition, i.e., carrier relaxation to the dark $1s(g)$ state vs activation from $1s(g)$ to higher energy levels which lead to the unusual excitation-dependent lifetime broadening of the bright state $1s(u)$. This is consistent with the temperature-dependent nonmonotonic dephasing time of $1s(u)$ state extracted in coherent transient spectroscopy measurements [26].

II. METHODS

A. Sample preparation

The sample we study is Co-Mo-catalyst-grown SWNTs of mostly (6,5) and (7,5) chiralities embedded in a 50-μm-thick freestanding sodium dodecylbenzenesulfonate (SDBS) film, which is air dried to optical quality from a D_2O solution of SDBS-dispersed SWNTs. The preparation basically follows procedures from Ref. [31]. The absorption spectrum of the film at room temperature is shown in Fig. 1(c). It exhibits clear excitonic signature of absorption peaks from (6,5) and (7,5) nanotubes, which is consistent with prior measurement of high-quality nanotube samples and corroborates the inclusion of the nanotubes into SDBS matrix [22,32]. SDBS not only ensures the transparency of the polymer matrix in THz range [33], but serves as a surfactant to effectively reduce SWNT bundles which are found to greatly weaken optical qualities of carbon nanotubes, such as PL quenching, extremely rapid carrier relaxation, and large-spectrum linewidth broadening, etc. [10,34].

B. Experimental setup

We perform optical pump and THz probe spectroscopic measurement, which is driven by a 1-kHz Ti:sapphire regenerative amplifier with 40-fs pulse duration and 800-nm central wavelength. The majority of the output is used to pump an optical parametric amplifier to generate visible laser pulses at 572 nm for resonant excitation of excitonic E_{22} band of (6,5) nanotubes as shown in Fig. 1. The other part of the output is used to generate and detect phase-locked THz field transients through optical rectification and electro-optic sampling in two 1-mm-thick $\langle 110 \rangle$-oriented ZnTe crystals, respectively. The relative time delay between THz field and sampling beam is defined as the gate time t. The produced THz pulses, used as a probe, exhibit a faithful spectral width from 0.5 to 2.5 THz with a signal-to-noise ratio over 5000 at the peak of the spectrum. The sample is mounted onto a 2.5-mm-diameter copper aperture to ensure uniform photoexcitation of the sample, and the other copper aperture with the same diameter is used as a reference to measure free propagation of THz pulses. The sample and apertures are placed into a vacuum cryostat in order to measure the sample at low temperature down to 5 K. The THz part of the setup is enclosed in a dry N_2 gas purge box to get rid of THz absorption by water vapor.

C. THz data analysis

In order to obtain transient dynamics of THz conductivity and dielectric function of the sample after photoexcitation, we

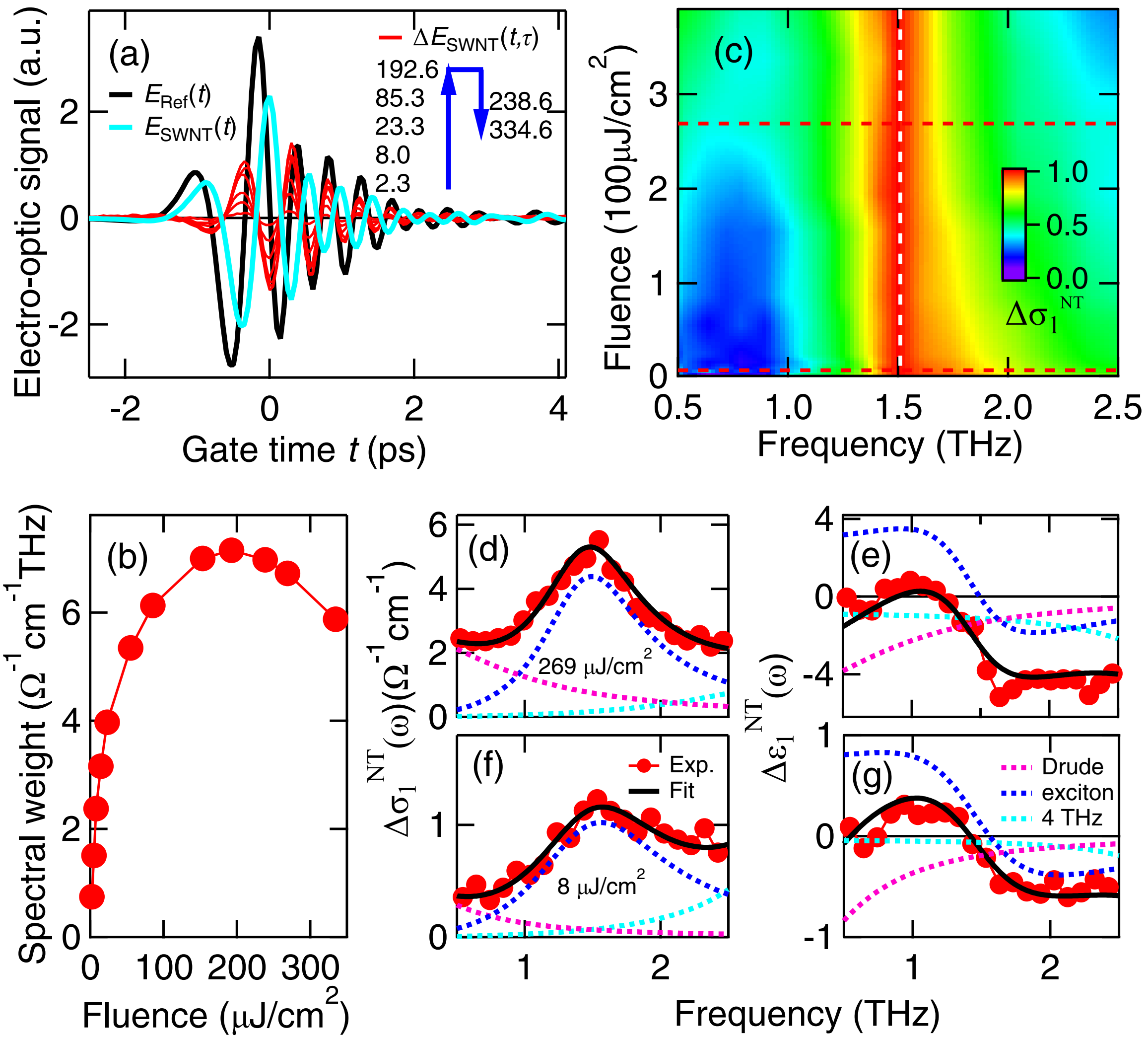

FIG. 2. Fluence-dependent spectral linewidth broadening. (a) Raw THz fields in time domain transmitted through clear aperture $E_{\mathrm{Ref}}(t)$ (black), static sample without pump $E_{\mathrm{SWNT}}(t)$ (cyan), and pump-induced THz field changes $\Delta E_{\mathrm{SWNT}}(t,\tau)$ (red) after 572-nm resonant excitation for several selected fluences from 2.3 to 334.6 $\mu\mathrm{J/cm}^2$ at $T = 5$ K and pump-probe delay time $\tau = 0.5$ ps. The blue arrows indicate the amplitude change of $\Delta E_{\mathrm{SWNT}}(t,\tau)$, which increases from 2.3 $\mu\mathrm{J/cm}^2$ to the maximum at 192.6 $\mu\mathrm{J/cm}^2$, and afterward it starts to decrease with further increasing fluence to 334.6 $\mu\mathrm{J/cm}^2$. $E_{\mathrm{Ref}}(t)$ and $E_{\mathrm{SWNT}}(t)$ are scaled down by 1/20 for clarity. (b) The integrated spectral weight of $\Delta\sigma_1^{\mathrm{NT}}(\omega)$ from 0.5 to 2.5 THz as a function of pump fluence. (c) The 2D false-color plot of $\Delta\sigma_1^{\mathrm{NT}}(\omega)$ as a function of fluence. The amplitude of $\Delta\sigma_1^{\mathrm{NT}}(\omega)$ for all fluences is normalized in order to more intuitively compare the peak linewidth of the $1s(g) \rightarrow 1s(u)$ intraexcitonic transition. The two red dashed lines mark the position of two pump fluences (8 and 269 $\mu\mathrm{J/cm}^2$) with their fitting details shown in (d)–(g). The THz spectra $\Delta\sigma_1^{\mathrm{NT}}(\omega)$ and $\Delta\varepsilon_1^{\mathrm{NT}}(\omega)$ for (d), (e) 269 $\mu\mathrm{J/cm}^2$ and (f), (g) 8 $\mu\mathrm{J/cm}^2$ (red dots), respectively, are fitted very well by the analytical model (black solid lines) from Eq. (1), which is the sum of $1s(g) \rightarrow 1s(u)$ intraexcitonic transition (blue dashed lines), Drude free carriers (magenta dashed lines), and 4-THz absorption band (cyan dashed lines).

firstly measure THz fields in time domain through the clear aperture $E_{\mathrm{Ref}}(t)$, static sample $E_{\mathrm{SWNT}}(t)$, and pump-induced THz field change $\Delta E_{\mathrm{SWNT}}(t,\tau)$ at a pump-probe delay time τ, as shown in Figs. 2(a) and 3(a). The phase-sensitive nature of the time-domain THz spectroscopy technique ensures the calculation of both real and imaginary parts of the conductivity and dielectric function without the use of Kramers-Kronig relations [28]. Specifically, through the fast Fourier transformation and Fresnel equations, the complex-valued static transmission coefficient through the sample can be calculated as $T(\omega) = E_{\mathrm{SWNT}}(\omega)/E_{\mathrm{Ref}}(\omega)$, from which the static refractive index $\tilde{n}(\omega)$, dielectric function $\tilde{\varepsilon}(\omega) = [\tilde{n}(\omega)]^2$, and conductivity $\tilde{\sigma}(\omega) = i[1 - \tilde{\varepsilon}(\omega)]\varepsilon_0\omega$ in THz range are obtained [28]. Similarly, from the photoexcited transient transmission coefficient $T'(\omega,\tau) = [E_{\mathrm{SWNT}}(\omega) + \Delta E_{\mathrm{SWNT}}(\omega,\tau)]/E_{\mathrm{Ref}}(\omega)$, the photoexcited transient THz spectra $\tilde{\sigma}'(\omega,\tau)$ and $\tilde{\varepsilon}'(\omega,\tau)$, and their pump-induced changes $\Delta\tilde{\sigma}(\omega,\tau) = \tilde{\sigma}'(\omega,\tau) - \tilde{\sigma}(\omega)$ and $\Delta\tilde{\varepsilon}(\omega,\tau) = \tilde{\varepsilon}'(\omega,\tau) - \tilde{\varepsilon}(\omega)$, are thus obtained. For simplicity, the term τ is omitted in the expression of $\Delta\tilde{\sigma}(\omega)$ and $\Delta\tilde{\varepsilon}(\omega)$ when no confusion arises. Note the THz spectra calculated above are actually the averaged effective values from a small portion of nanotubes embedded in bulky SDBS material. Therefore, effective medium approximation needs to be applied in order to calculate the pure contribution from carbon nanotubes [23,28]. To do so, the nanotube space filling ratio (FR) of the sample ~0.88% is calculated through

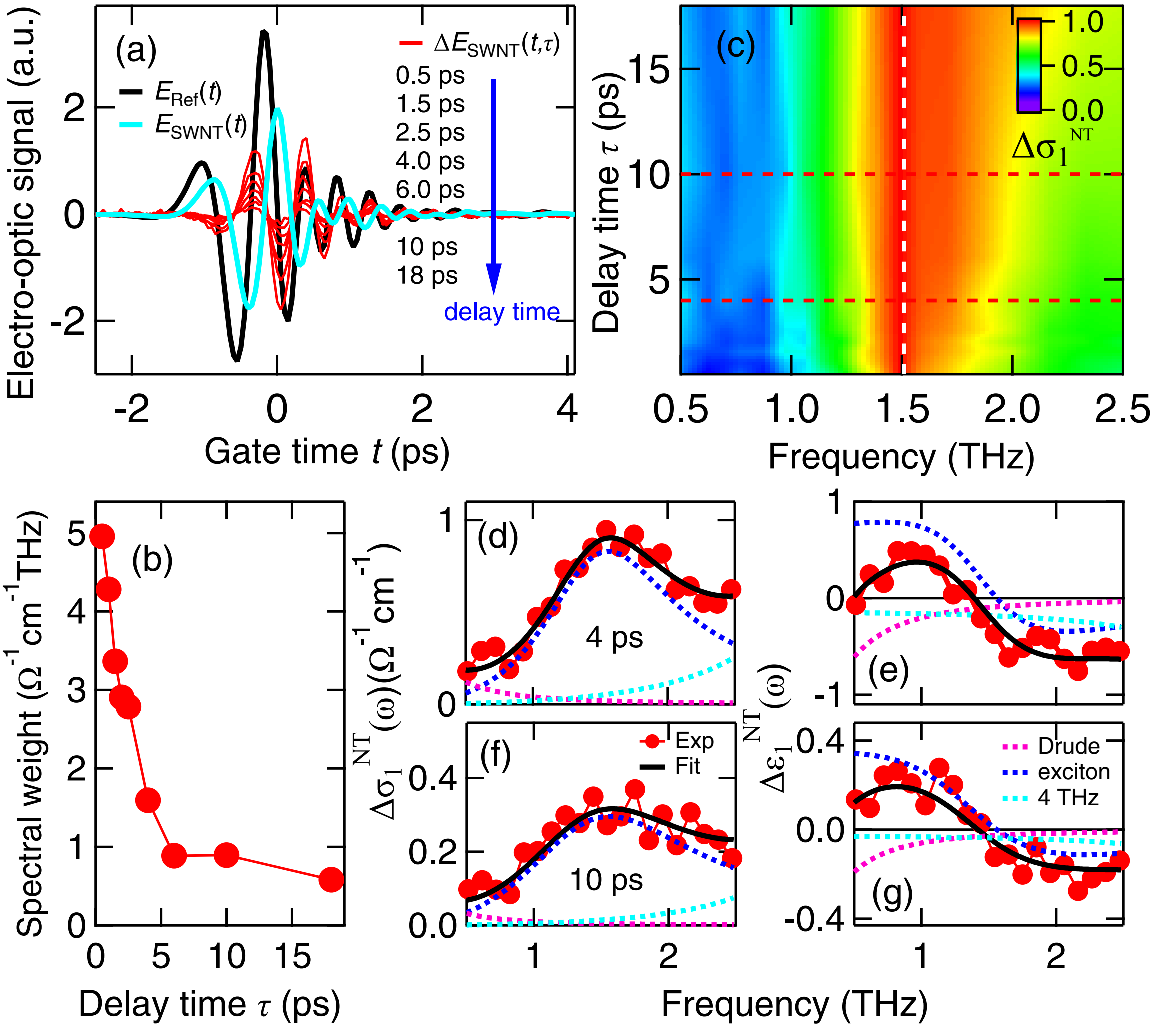

FIG. 3. Time-dependent spectral linewidth broadening. (a) Raw THz fields in time domain transmitted through clear aperture $E_{\rm Ref}(t)$ (black), static sample without pump $E_{\rm SWNT}(t)$ (cyan), and the pump-induced THz field changes $\Delta E_{\rm SWNT}(t,\tau)$ (red) after 572-nm resonant excitation for several pump-probe delay times τ from 0.5 to 18 ps, at $T = 5$ K and 48 μJ/cm^2. The blue arrow indicates that the amplitude of $\Delta E_{\rm SWNT}(t,\tau)$ decreases monotonically with τ from 0.5 to 18 ps. $E_{\rm Ref}(t)$ and $E_{\rm SWNT}(t)$ are scaled down by 1/20 for clarity. (b) Integrated spectral weight of $\Delta\sigma_1^{\rm NT}(\omega)$ from 0.5 to 2.5 THz as a function of τ. (c) The 2D false-color plot of $\Delta\sigma_1^{\rm NT}(\omega)$ as a function of delay time τ. The amplitude of $\Delta\sigma_1^{\rm NT}(\omega)$ for all delay times is normalized in order to compare more intuitively the peak linewidth. The two red dashed lines mark the position of two delay times (4 and 10 ps) with their fitting details shown in (d)–(g). The THz spectra $\Delta\sigma_1^{\rm NT}(\omega)$ and $\Delta\varepsilon_1^{\rm NT}(\omega)$ for (d), (e) 4 ps and (f), (g) 10 ps (red dots), respectively, are fitted very well by the analytical model (black solid lines) from Eq. (1), which is the sum of $1s(g) \rightarrow 1s(u)$ intraexcitonic transition (blue dashed lines), Drude free carriers (magenta dashed lines), and 4-THz absorption band (cyan dashed lines).

absorption measurement, from where a simple relationship of $\Delta\tilde{\varepsilon}^{\rm NT}(\omega) = \Delta\tilde{\varepsilon}(\omega)/{\rm FR}$ is obtained for ${\rm FR} \ll 1$ as shown in Refs. [23,35,36], and the equation for $\Delta\tilde{\sigma}^{\rm NT}(\omega)$ takes the same mathematical relationship. In our study, the real parts of the THz spectra, i.e., $\Delta\sigma_1^{\rm NT}(\omega)$ and $\Delta\varepsilon_1^{\rm NT}(\omega)$ are presented, which measure the dissipative and inductive responses of carriers in nanotubes, respectively.

D. Theoretical fitting

The experimentally obtained THz spectra can be fitted very well by a theoretical model consisting of three components, which assumes the coexistence of excitons, free charge carriers, and 4-THz absorption band:

$$\tilde{\varepsilon}^{\rm NT}(\omega) = \tilde{\varepsilon}_X(\omega) + \tilde{\varepsilon}_{\rm Drude}(\omega) + \tilde{\varepsilon}_\alpha(\omega). \qquad (1)$$

The corresponding conductivity can be calculated from $\tilde{\sigma}^{\rm NT}(\omega) = i[1 - \tilde{\varepsilon}^{\rm NT}(\omega)]\varepsilon_0\omega$ [23,37]. The first term in Eq. (1) accounts for the $1s(g) \rightarrow 1s(u)$ intraexcitonic transition $\tilde{\varepsilon}_X(\omega) = \varepsilon_\infty + f(\Delta n_X e^2/\varepsilon_0 m_X)/(\omega_X^2 - \omega^2 - i\omega\Gamma)$. Here ε_0 and ε_∞ are the vacuum and background electrical permittivity, respectively, $\Delta n_X = n_{1s(g)} - n_{1s(u)}$ is the population difference between the two states involved in transition, e is electron charge, Γ is intraexcitonic transition linewidth, $m_X = 0.068 m_0$ (m_0 is electron mass) is exciton effective mass taken from Ref. [38], ω is frequency, ω_X is the resonant frequency of the intraexcitonic transition found to be $\sim$1.5 THz, and f is the oscillator strength of the intraexcitonic transition determined to be 0.79 [23]. In the fitting, ε_0, ε_∞, e, m_X, and f are constant. Δn_X, ω_X, and Γ are varied to reproduce experimental results. The second term $\tilde{\varepsilon}_{\rm Drude}(\omega) = -(n_e e^2/\varepsilon_0 m_e)/(\omega^2 +$

$i\omega\gamma$) describes the Drude free charge carriers. $m_e = 0.131m_0$ is electron effective mass taken from Ref. [38], γ and n_e are free-carrier linewidth and density, respectively. In the fitting, γ and n_e are varied to reproduce experimental results, and other parameters are constant. The third term describing the 4-THz absorption band has the same mathematical form as the first one, i.e., $\tilde{\varepsilon}_\alpha(\omega) \sim A/(\omega_\alpha^2 - \omega^2 - i\omega\Gamma_\alpha)$, where A is a prefactor, ω_α and Γ_α are the oscillator resonant frequency and linewidth, respectively, but the resonant frequency ω_α is at 4 THz instead, as confirmed in many prior studies [35,39–41] as well as our fitting. A and Γ_α are varied to reproduce the experimental results, which are trivial and not reported in the current study. The fitting results of Γ, γ, Δn_X, and n_e as a function of delay time and pump fluence are plotted in Fig. 4.

The fact that each component has a distinct spectral line shape and both conductivity and dielectric function line shapes need to be simultaneously fitted guarantees the best set of fitting parameters is unique. A fitting will not match with experimental results if any component is missing or their respective spectral weight is not set correctly. Therefore, the extracted fluence-dependent and time-dependent carrier densities and spectral linewidths allow us to faithfully study ultrafast carrier dynamics of photogenerated lowest-lying excitons and free charge carriers. Data with individual fitting components and fitting validity are discussed next.

III. RESULTS AND DISCUSSION

Typical ultrafast pump-induced THz spectra of $\Delta\sigma_1^{\mathrm{NT}}(\omega)$ and $\Delta\varepsilon_1^{\mathrm{NT}}(\omega)$ (red dots), carrying information of photogenerated carrier dynamics of SWNTs, are shown in Figs. 2(d)–2(g) and Figs. 3(d)–3(g). A pronounced photoinduced absorptive peak appears in $\Delta\sigma_1^{\mathrm{NT}}(\omega)$ near ~1.5 THz (6.2 meV), and an inductive response near the same frequency is clearly visible in $\Delta\varepsilon_1^{\mathrm{NT}}(\omega)$. These two features are characteristic of a photoinduced THz oscillator with a resonant frequency of ~1.5 THz from the internal excitonic transition $1s(g) \rightarrow 1s(u)$, which is marked by red arrows in Fig. 1(b) and is reported in detail in our prior study [23]. In addition, the finite conductivity $\Delta\sigma_1^{\mathrm{NT}}(\omega)$ persisting towards low frequency and the negatively offset dielectric function $\Delta\varepsilon_1^{\mathrm{NT}}(\omega)$ indicate an additional Drude spectral weight, from coexisting photogenerated free charge carriers [12,23]. Lastly, the contribution to the THz spectra includes a broad absorption band centered at ~4 THz, which is outside our THz probe spectral range. Although it cannot be completely observed from the THz spectral line shape, it is clearly identified by fitting the theoretical model as described in Methods. The 4-THz absorption band appears to be "universal" in all SWNTs and the origin is still debated [35,39–41].

Figure 2 presents the ultrafast THz raw data and extracted THz spectra as a function of pump fluence. In Fig. 2(a), the pump-induced THz field change $\Delta E_{\mathrm{SWNT}}(t,\tau)$ (red curves) exhibits a nonmonotonic behavior. It initially increases by increasing pump fluence from 2.3 to 192.6 $\mu\mathrm{J/cm}^2$, where it reaches its maximum. Afterward, it starts to decrease when pump fluence is further increased to 334.6 $\mu\mathrm{J/cm}^2$. This interesting nonmonotonic variation can be explained as follows. When pump fluence is below a critical value $I_c \sim 192.6\ \mu\mathrm{J/cm}^2$ in the case of E_{22} resonant excitation at 572 nm, the photogenerated excitons primarily populate in the lowest-lying dark exciton state $1s(g)$ [42], which leads to the rapid signal increase from $1s(g) \rightarrow 1s(u)$ intraexcitonic transition with increasing pump fluence. However, above I_c, photogenerated excitons have a greater probability to populate at the lowest-lying bright exciton state $1s(u)$, due to photoinduced electronic heating of the many-body system, and therefore the $1s(g) \rightarrow 1s(u)$ intraexcitonic transition is weakened. A similar nonmonotonic behavior has been reported in our prior study with 800-nm off-resonant excitation, in which a smaller $I_c \sim 130\ \mu\mathrm{J/cm}^2$ is found [23], because off-resonant

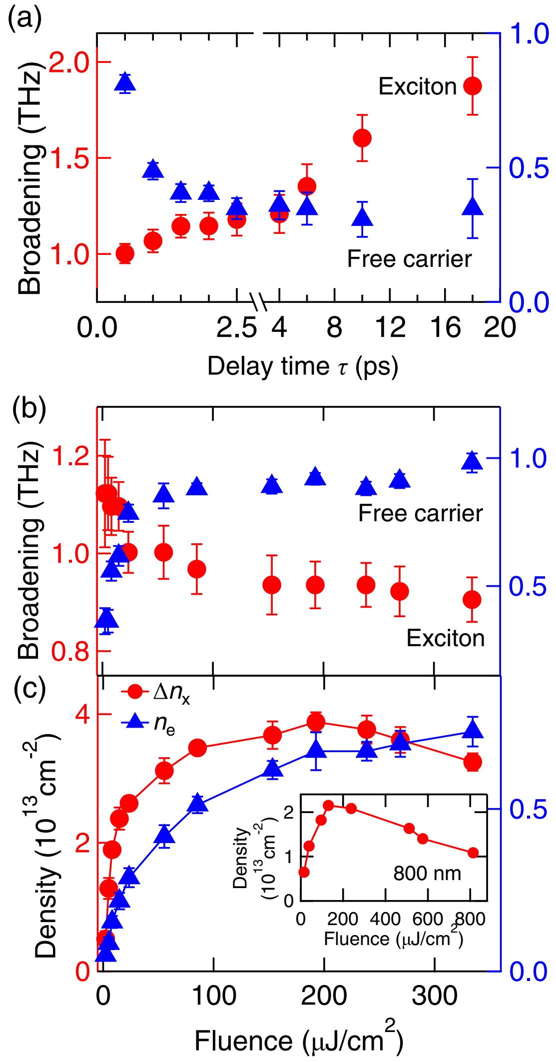

FIG. 4. (a) Temporal evolution of photoinduced spectral linewidths of excitons (red dots, left axis) and free carriers (blue triangles, right axis) after 572-nm resonant photoexcitation at $T = 5$ K and 48 $\mu\mathrm{J/cm}^2$. The error bar indicates fitting uncertainty. (b) The linewidth of excitons (red dots, left axis) and free carriers (blue triangles, right axis) as a function of pump fluence after 572-nm resonant excitation at $T = 5$ K and delay time $\tau = 0.5$ ps. (c) The density of free carriers n_e (blue triangles, right axis) and the density difference of the two excitonic states $\Delta n_X = n_{1s(g)} - n_{1s(u)}$ (red dots, left axis) after 572-nm resonant photoexcitation at $T = 5$ K and $\tau = 0.5$ ps. The inset shows Δn_X under the same lab conditions but with 800-nm off-resonant photoexcitation instead.

excitation should create a hotter electronic distribution and be easier to thermally populate the 1$s(u)$ state. This statement is further corroborated by exciton density dependence to be shown in Fig. 4(c).

The conductivity $\Delta\sigma_1^{\mathrm{NT}}(\omega)$ extracted from Fig. 2(a) is presented in Fig. 2(b) in the form of an integrated spectral weight from 0.5 to 2.5 THz, i.e., $\int_{0.5}^{2.5}\Delta\sigma_1^{\mathrm{NT}}(\omega)d\omega$, as a function of fluence, which follows the variation of $\Delta E_{\mathrm{SWNT}}(t,\tau)$. This consolidates our interpretation of photoinduced THz field transmission as conductivity changes. More importantly, two salient features can be seen from a 2D false-color plot of normalized $\Delta\sigma_1^{\mathrm{NT}}(\omega)$ in Fig. 2(c). We emphasize two key observations. First, the absorption peak of $\Delta\sigma_1^{\mathrm{NT}}(\omega)$ near 1.5 THz, which originates from the intraexcitonic transition, does not exhibit noticeable spectral drift as marked by the white dashed line, indicating the resonant frequency of the intraexcitonic transition is stable over the whole range of pump fluence from 2.3 to 334.6 $\mu\mathrm{J/cm^2}$. In our prior study of off-resonant photoexcitation at 800 nm [23], we found that coexisting free carriers could redshift the intraexcitonic transition peak when their density is comparable to that of excitons, due to the interaction of free carriers and excitons leading to the energy renormalization of the excitonic states. The peak position stability under high-density excitons observed here with resonant photoexcitation otherwise attests to the strong Coulomb binding and indicates the density of free carriers is still much smaller than that of excitons, as to be confirmed in Fig. 4(c). Second, most intriguingly, the transition peak linewidth narrows gradually with increasing pump fluence. This can be seen instructively from the 2D plot or from detailed THz spectra fitting shown in Figs. 2(d)–2(f). The dashed blue lines for lower fluence (8 $\mu\mathrm{J/cm^2}$) are clearly broader than that of higher fluence (269 $\mu\mathrm{J/cm^2}$). Because this observation is based on our fitting, we want to make sure the fitting results are faithful. To kill any ambiguity, we also have tried to intentionally fit the data, particularly the intraexcitonic transition broadening, with the "normal" trend one would expect at first glance, i.e., exciton broadening increases with fluence and decreases with time, but we finally found we could not fit our data this way. More importantly, our fitting results, particularly the anomalous exciton broadening dynamics, can be fully supported by many SWNT exciton studies from other perspectives, such as the temperature-dependent PL and the exciton dephasing measurement to be discussed later. Therefore, we believe the reported fitting results are faithful.

Figure 3 plots the THz raw data and extracted THz spectra as a function of pump-probe delay time τ in the same manner as Fig. 2. $\Delta E_{\mathrm{SWNT}}(t,\tau)$ in Fig. 3(a) exhibits a monotonic behavior, which decreases with delay time from 0.5 to 18 ps. This can be easily understood as the relaxation of photogenerated exciton and free-carrier densities, leading to a decreased THz transient conductivity. The integrated spectral weight in Fig. 3(b) similarly follows $\Delta E_{\mathrm{SWNT}}(t,\tau)$. Two similar features are observed in the 2D false-color plot in Fig. 3(c). First, the spectral position of the transition peak has no noticeable shift with delay time as marked by the white dashed line. Second, the transition peak linewidth increases with delay time markedly, which can be seen instructively from the 2D plot or from the detailed THz spectra fitting shown in Figs. 3(d)–3(g). The intraexcitonic transition linewidth for earlier delay time [4 ps in Fig. 3(d)] is clearly narrower than that of larger delay time [10 ps in Fig. 3(f)]. Note the asymmetric conductivity line shape shown in Figs. 2 and 3 arises mostly from the asymmetric feature of the intraexcitonic transition itself as shown by the blue dashed lines or in other excitonic study [28]. The 4-THz absorption band also makes some contribution at higher energy side. These experiments clearly show that the transition peak linewidth can be tuned by both the pump fluence and delay time.

To put our observation of the ultrafast dynamics of carriers and spectral linewidths on a solid footing, we fit the experimentally determined THz spectra by the theoretical model of Eq. (1). This allows us to faithfully extract the spectral linewidths and densities of excitons and free carriers as a function of delay time or pump fluence, as shown in Fig. 4. The linewidth of free carriers (blue triangles) decreases by 50%, from ~0.8 to ~0.4 THz, when the delay time is increased from 0.5 to 18 ps, as in Fig. 4(a). This is consistent with typical photoinduced carrier dynamics in semiconductors such as GaAs [43]. In contrast, the excitonic spectral linewidth (red dots) exhibits an opposite trend, which increases by 80%, from ~1.0 to ~1.8 THz by decreasing the transient population although it may seem contradictory to what one would normally expect from population dependence. Nevertheless, this observation is in accord with results from fluence-dependent spectral linewidth data as shown in Fig. 4(b), which corroborates the validity of the above observation. By increasing pump fluence from 2.3 to 334.6 $\mu\mathrm{J/cm^2}$, the transient lattice temperature T_l and exciton density increase, and the exciton transition linewidth decreases from ~1.1 to ~0.9 THz accordingly. The linewidth of free carriers, however, increases with increasing fluence, as expected.

In order to explain the observed anomalous variations of excitonic spectral linewidth, we firstly survey the relevant experimental results in the literature. Graham *et al.* [26] observed that in semiconducting SWNTs, the dark exciton state 1$s(g)$ plays a very critical role in the temperature-dependent dephasing time (i.e., inversely proportional to spectral linewidth) of the bright exciton state 1$s(u)$, which is just a few meV above 1$s(g)$. They found a crossover behavior that the 1$s(u)$ spectral linewidth initially decreases when lattice temperature is decreased from 292 to ~70 K, where it reaches its minimum. Then it starts to increase when the lattice temperature is further reduced from 70 to 2.5 K. On the one hand, lowering temperature from 292 to 70 K one lowers phonon population and weakens phonon-exciton scattering, which yields a larger dephasing time and smaller spectral linewidth. On the other hand, the increase of the spectral linewidth from 70 to 2.5 K cannot be attributed to phonon-exciton scattering, but is instead associated with another competing mechanism that gets dominated below 70 K, i.e., the accelerated relaxation of 1$s(u)$ excitons to the lower 1$s(g)$ state. When the lattice temperature is lowered below 70 K, the thermal energy k_BT (k_B is the Boltzmann constant) is getting smaller than the gap of the intraexcitonic transition ~1.5 THz (6.2 meV) as shown in our study and several others [20,24,44], so that the 1$s(u)$ state is no longer thermally accessible for excitons in 1$s(g)$ state and thus the overall relaxation rate of 1$s(u)$ excitons to 1$s(g)$ state is accelerated. Therefore, $1s(u)$ dephasing time decreases quickly and spectral linewidth increases due to such lifetime broadening with decreasing temperature from 70 to 2.5 K. In addition, temperature-dependent PL measurements in SWNTs see a similar nonmonotonic behavior near ∼20–80 K depending on chiralities and sample details [16,18,45,46], in which the suppressed PL intensity at low temperature is attributed to the accelerated relaxation of $1s(u)$ bright excitons to the $1s(g)$ dark state.

A physical picture emerges for the observed transition peak linewidth vs the pump fluence and delay time. The observation of monotonic variation of excitonic spectral linewidth [red dots, Figs. 4(a) and 4(b)] can be satisfactorily explained as follows: after 572-nm resonant photoexcitation, excitons are created predominately at $1s(g)$ and $1s(u)$ states within 100 fs [17,47]. The photoinduced transient temperature T_l is elevated, yet still below ∼70 K, so that the lifetime broadening is suppressed. This leads to a reduced spectral linewidth. The subsequent relaxation process decreases T_l and recovers the original spectral linewidth as shown in Fig. 4(a). This is also consistent with the pump fluence narrowing seen in Fig. 4(b) where the spectral linewidth starts to decrease with further increasing photoexcitation or temperature. Here we see a nearly monotonic decrease of exciton linewidth as pump fluence increases, which implies that the pump-induced transient T_l of the sample is still no more than the crossover temperature of 70 K up to the maximum pump fluence of 334.6 $\mu\mathrm{J/cm}^2$, or we would see a nonmonotonic variation of the spectral linewidth. Finally, it should be noted that although the spectral linewidth of the intraexcitonic transition relies on that of both $1s(g)$ and $1s(u)$ states, the $1s(g)$ dark state does not optically couple to the ground state, so it has much longer dephasing time and narrower linewidth compared to that of $1s(u)$ state. Therefore, the observed spectral linewidth of the $1s(g) \rightarrow 1s(u)$ intraexcitonic transition predominately counts on the $1s(u)$ state.

The fluence-dependent carrier densities are plotted in Fig. 4(c). The density difference of excitons Δn_X exhibits a distinct nonmonotonic variation with increasing fluence, which peaks at $I_c \sim 192.6\ \mu\mathrm{J/cm}^2$ and followed by a reduction when the fluence is further increased to 334.6 $\mu\mathrm{J/cm}^2$, consistent with raw data of THz field in Fig. 2(a). However, the free-carrier density exhibits a sublinear relationship with fluence, as expected. In addition, the linewidths of free carriers and excitons exhibit no significant variation above I_c as shown in Fig. 4(b). These indicate the reduction of Δn_X above I_c is not due to exciton annihilation, but rather from the evolution from a predominate $1s(g)$ dark exciton population at low pump fluence to the occupancy of both the $1s(g)$ dark and $1s(u)$ bright exciton states at higher fluence with gradually elevated electronic temperature [23].

As an example of off-resonant photoexcitation at 800 nm, Δn_X shows a nonmonotonic variation in the inset of Fig. 4(c). However, both the exciton saturation density and the crossover fluence $I_c \sim 130\ \mu\mathrm{J/cm}^2$ of 800-nm off-resonant photoexcitation are lower than that of 572-nm resonant photoexcitation, because off-resonant excitation is expected to induce more electronic heating and free carriers into the many-body system. Note that the resonant photoexcitation used in the experiment is preferred and expected to generate minimum free carriers comparing to off-resonant photoexcitation. This allows the clearer observation of the excitation-induced excitonic linewidth narrowing with dominant exciton population.

Finally, we note that the pump-induced THz conductivity of internal excitonic states arises from two competing processes of the absorption and induced emission within the boson approximation. The phase space filling can also contribute to these two competing processes at the high exciton density regime since exciton Bohr radius is comparable to interparticle spacing. Note that these two processes are naturally taken into account in our theoretical modeling as positive or negative oscillator strength.

IV. CONCLUSION

We perform the measurement of the spectral linewidths of excitons and free carriers under intense resonant photoexcitation using ultrafast THz probes of internal excitonic quantum levels. We clearly see anomalous variation of excitonic spectral linewidth after photoexcitation, absent in free carriers. The several-meV energy gap between the dark $1s(g)$ and bright $1s(u)$ ground states is found to play a crucial role in the observed anomalous variation of the linewidth. These results shine light on better understanding many-body quantum states and photophysics required for development of optoelectronic devices involving excitonic transitions of SWNTs. This offer perspectives of exploring related elementary excitations in other complex materials such as superconductors [48], magnetic [49], and topological materials [50].

ACKNOWLEDGMENT

This work was supported by the National Science Foundation Award No. 1611454.

---

[1] R. Saito, A. R. T. Nugraha, E. H. Hasdeo, N. T. Hung, and W. Izumida, Top. Curr. Chem. **375**, 7 (2017).

[2] C. Biswas and Y. H. Lee, Adv. Funct. Mater. **21**, 3806 (2011).

[3] C. T. White and J. W. Mintmire, J. Phys. Chem. B **109**, 52 (2005).

[4] S. Kilina and S. Tretiak, Adv. Funct. Mater. **17**, 3405 (2007).

[5] M. F. L. De Volder, S. H. Tawfick, R. H. Baughman, and A. J. Hart, Science **339**, 535 (2013).

[6] N. M. Gabor, Z. Zhong, K. Bosnick, J. Park, and P. L. McEuen, Science **325**, 1367 (2009).

[7] W. Walden-Newman, I. Sarpkaya, and S. Strauf, Nano Lett. **12**, 1934 (2012).

[8] F. Wang, G. Dukovic, L. E. Brus, and T. F. Heinz, Science **308**, 838 (2005).

[9] V. Perebeinos, J. Tersoff, and P. Avouris, Phys. Rev. Lett. **92**, 257402 (2004).

[10] F. Wang, G. Dukovic, L. E. Brus, and T. F. Heinz, Phys. Rev. Lett. **92**, 177401 (2004).

[11] J. Maultzsch, R. Pomraenke, S. Reich, E. Chang, D. Prezzi, A. Ruini, E. Molinari, M. S. Strano, C. Thomsen, and C. Lienau, Phys. Rev. B **72**, 241402(R) (2005).

[12] R Huber, R. A. Kaindl, B. A. Schmid, and D. S. Chemla, Phys. Rev. B **72**, 161314(R) (2005).

[13] L. Kappei, J. Szczytko, F. Morier-Genoud, and B. Deveaud, Phys. Rev. Lett. **94**, 147403 (2005).

[14] S. B. Nam, D. C. Reynolds, C. W. Litton, R. J. Almassy, T. C. Collins, and C. M. Wolfe, Phys. Rev. B **13**, 761 (1976).

[15] H. Zhao and S. Mazumdar, Phys. Rev. Lett. **93**, 157402 (2004).

[16] V. Perebeinos, J. Tersoff, and P. Avouris, Nano Lett. **5**, 2495 (2005).

[17] Y. Murakami and J. Kono, Phys. Rev. Lett. **102**, 037401 (2009).

[18] I. B. Mortimer and R. J. Nicholas, Phys. Rev. Lett. **98**, 027404 (2007).

[19] S. Zaric, G. N. Ostojic, J. Shaver, J. Kono, O. Portugall, P. H. Frings, G. L. J. A. Rikken, M. Furis, S. A. Crooker, X. Wei, V. C. Moore, R. H. Hauge, and R. E. Smalley, Phys. Rev. Lett. **96**, 016406 (2006).

[20] A. Srivastava, H. Htoon, V. I. Klimov, and J. Kono, Phys. Rev. Lett. **101**, 087402 (2008).

[21] G. N. Ostojic, S. Zaric, J. Kono, V. C. Moore, R. H. Hauge, and R. E. Smalley, Phys. Rev. Lett. **94**, 097401 (2005).

[22] J. Wang, M. W. Graham, Y. Ma, G. R. Fleming, and R. A. Kaindl, Phys. Rev. Lett. **104**, 177401 (2010).

[23] L. Luo, I. Chatzakis, A. Patz, and J. Wang, Phys. Rev. Lett. **114**, 107402 (2015).

[24] J. Shaver, J. Kono, O. Portugall, V. Krstić, G. L. J. A. Rikken, Y. Miyauchi, S. Maruyama, and V. Perebeinos, Nano Lett. **7**, 1851 (2007).

[25] C. D. Spataru, S. Ismail-Beigi, R. B. Capaz, and S. G. Louie, Phys. Rev. Lett. **95**, 247402 (2005).

[26] M. W. Graham, Y. Ma, A. A. Green, M. C. Hersam, and G. R. Fleming, J. Chem. Phys. **134**, 034504 (2011).

[27] I. Sarpkaya, Z. Zhang, W. Walden-Newman, X. Wang, J. Hone, C. W. Wong, and S. Strauf, Nat. Commun. **4**, 2152 (2013).

[28] J. Lloyd-Hughes and T.-I. Jeon, J. Infrared, Millimeter, Terahertz Waves **33**, 871 (2012).

[29] L. Luo, L. Men, Z. Liu, Y. Mudryk, X. Zhao, Y. Yao, J. M. Park, R. Shinar, J. Shinar, K.-M. Ho, I. E. Perakis, J. Vela, and J. Wang, Nat. Commun. **8**, 15565 (2017).

[30] M. J. Kann, A. M. Kriman, and D. K. Ferry, Phys. Rev. B **41**, 12659 (1990).

[31] N. Minami, Y. Kim, K. Miyashita, S. Kazaoui, and B. Nalini, Appl. Phys. Lett. **88**, 093123 (2006).

[32] S. M. Bachilo, M. S. Strano, C. Kittrell, R. H. Hauge, R. E. Smalley, and R. B. Weisman, Science **298**, 2361 (2002).

[33] T. Ogawa, S. Watanabe, N. Minami, and R. Shimano, Appl. Phys. Lett. **97**, 041111 (2010).

[34] M. J. O'Connell, S. M. Bachilo, C. B. Huffman, V. C. Moore, M. S. Strano, E. H. Haroz, K. L. Rialon, P. J. Boul, W. H. Noon, C. Kittrell, J. Ma, R. H. Hauge, R. B. Weisman, and R. E. Smalley, Science **297**, 593 (2002).

[35] T. Kampfrath, L. Perfetti, K. Volkmann, C. M. Aguirre, P. Desjardins, R. Martel, C. Frischkorn, and M. Wolf, Phys. Status Solidi B **244**, 3950 (2007).

[36] F. J. Garcia-Vidal, J. M. Pitarke, and J. B. Pendry, Phys. Rev. Lett. **78**, 4289 (1997).

[37] R. A. Kaindl, D. Hagele, M. A. Carnahan, and D. S. Chemla, Phys. Rev. B **79**, 045320 (2009).

[38] A. Jorio, C. Fantini, M. A. Pimenta, R. B. Capaz, Ge. G. Samsonidze, G. Dresselhaus, M. S. Dresselhaus, J. Jiang, N. Kobayashi, A. Gruneis, and R. Saito, Phys. Rev. B **71**, 075401 (2005).

[39] A. Ugawa, A. G. Rinzler, and D. B. Tanner, Phys. Rev. B **60**, R11305(R) (1999).

[40] T. Jeon and K. Kim, J. Appl. Phys. **95**, 5736 (2004).

[41] N. Akima, Y. Iwasa, S. Brown, A. M. Barbour, J. Cao, J. L. Musfeldt, H. Matsui, N. Toyota, M. Shiraishi, H. Shimoda, and O. Zhou, Adv. Mater. **18**, 1166 (2006).

[42] J. J. Crochet, J. G. Duque, J. H. Werner, B. Lounis, L. Cognet, and S. K. Doorn, Nano Lett. **12**, 5091 (2012).

[43] M. C. Beard, G. M. Turner, and C. A. Schmuttenmaer, Phys. Rev. B **62**, 15764 (2000).

[44] R. Matsunaga, K. Matsuda, and Y. Kanemitsu, Phys. Rev. Lett. **101**, 147404 (2008).

[45] J. G. Duque, C. E. Hamilton, G. Gupta, S. A. Crooker, J. J. Crochet, A. Mohite, H. Htoon, K. A. DeFriend Obrey, A. M. Dattelbaum, and S. K. Doorn, ACS Nano **5**, 6686 (2011).

[46] R. Matsunaga, Y. Miyauchi, K. Matsuda, and Y. Kanemitsu, Phys. Rev. B **80**, 115436 (2009).

[47] C. Manzoni, A. Gambetta, E. Menna, M. Meneghetti, G. Lanzani, and G. Cerullo, Phys. Rev. Lett. **94**, 207401 (2005).

[48] X. Yang, C. Vaswani, C. Sundahl, M. Mootz, P. Gagel, L. Luo, J. H. Kang, P. P. Orth, I. E. Perakis, C. B. Eom, and J. Wang, Nat. Mater. **17**, 586 (2018); X. Yang, L. Luo, M. Mootz, A. Patz, S. L. Bud'ko, P. C. Canfield, I. E. Perakis, and J. Wang, Phys. Rev. Lett. **121**, 267001 (2018).

[49] J. Wang, G. A. Khodaparast, J. Kono, T. Slupinski, A. Oiwa, and H. Munekata, Physica E **20**, 412 (2004); A. Patz, T. Li, S. Ran, R. M. Fernandes, J. Schmalian, S. L. Bud'ko, P. C. Canfield, I. E. Perakis, and J. Wang, Nat. Commun. **5**, 3229 (2014).

[50] L. Luo, X. Yang, X. Liu, Z. Liu, C. Vaswani, D. Cheng, M. Mootz, X. Zhao, Y. Yao, C.-Z. Wang, K.-M. Ho, I. E. Perakis, M. Dobrowolska, J. K. Furdyna, and J. Wang, Nat. Commun. **10**, 607 (2019).